CrossMark
click for updates

Bio-ingredient assisted formation of porous TiO$_2$ for Li-ion battery electrodes†

Yi-Chun Chang,[a] Chih-Wei Peng,[a] Po-Chin Chen,[a] Chi-Young Lee[b] and Hsin-Tien Chiu*[a]

Macroporous TiO$_2$ was synthesized by using low-cost bio-ingredients as the pore forming templates. TiCl$_4$ in C$_2$H$_5$OH$_{(l)}$ containing NH$_4$OH$_{(aq.)}$ was polymerized in the presence of instant yeast and glucose. The organic–inorganic hybrid precursor was further processed to generate macroporous anatase TiO$_2$ (pore size: 2.5–3 μm) with mesopores (4–51 nm). The porous TiO$_2$ was coated with a thin layer of carbon by chemical vapour deposition to generate the hierarchical C/TiO$_2$ nanocomposite material. The porous products were investigated as anode materials for Li-ion batteries. The capacities of the hierarchical C/TiO$_2$ electrode material remained 180 mA h g^{-1} and 142 mA h g^{-1} under high charge/discharge rates of 5 C and 10 C, respectively. It demonstrated good cycling stability of 318 mA h g^{-1} at 0.1 C at various discharge–charge rates. The excellent performance is attributed to the high specific surface areas and open spaces of the C/TiO$_2$ allowing effortless intercalation/deintercalation of Li ions.

Introduction

With the rapid advancement of electronics and the demand for energy storage, advanced Li-ion batteries, with high energy and power densities, fast recharge rates, and good cyclic stability, are needed.[1,2] In addition, fabrication of the new devices should be low cost and free from toxic materials. Among various candidates for anode materials in Li-ion batteries, TiO$_2$ has attracted lots of attention due to its chemical stability, low cost, and environmentally safeness.[3–6] Compared to other anode materials such as graphite and Sn, TiO$_2$ shows negligible volume change during cycling and does not form harmful solid–electrolyte interface (SEI) layer.[7–9] However, TiO$_2$ has intrinsically low Li ion and electron conductivities. Among various TiO$_2$ phases, anatase has been investigated more due to its higher ion diffusion property, which is about an order of magnitude higher than the value of rutile, another common TiO$_2$ phase.[10–12] In order to solve these drawbacks, optimizing specific morphology and scaling down particle sizes have been attempted to minimize the Li ion diffusion pathways.[13–16] Furthermore, forming composites containing TiO$_2$ and conductive agents may provide feasible ways to improve the electron transport properties in the electrode.[17–20] Consequently, how to design suitable morphology and utilize

conductive material efficiently is a challenge for the development of better TiO$_2$ electrode for Li-ion batteries.

Materials with specific morphology might exhibit enhanced properties. Among them, porous structures are potentially useful due to their highly exposed skeleton, high specific surface area, and low bulk density.[21] Sacrificial templates are frequently employed to generate various porous structures. Common artificial templates, such as polystyrene spheres, which require multiple chemical reactions to obtain, are expensive. On the other hand, biotemplates displaying astonishingly sophisticated natural structures could be employed to generate porous inorganic structures.[22–24] The biotemplates could be as large as cell level organisms, such as prokaryotes (bacteria and fungi) and eukaryotes (animal and plant cells), as well as molecular level cell-derived subunits (protein, enzymes, and DNA).[25–31] In literature, yeast (*Saccharomyces cerevisiae*) assisted fabrications of porous inorganic structures are known.[32–36] Glucose assisted pore generation processes have been reported also.[37,38] Recently, we reported the fabrication of a novel channel-like porous TiO$_2$ by using living yeast cells as the templates.[39] The cells maintained their vitality in the reactions and created the TiO$_2$ with the unique morphology. The material was explored for potential Li-ion battery electrode application. In this study, we report a different porous TiO$_2$ fabrication process employing the same low cost bio-ingredients, yeast and glucose, as the sacrificial porogens *via* a simple sol–gel reaction route. All of the bio-ingredients used were environmental friendly, sustainable and easy to obtain. In this case, the physiological activities of the yeast were ceased due to the inhospitable environment for the cells. The as-fabricated TiO$_2$ contains both macro- and mesopores and demonstrates excellent Li-ion battery performance.

[a]*Department of Applied Chemistry, National Chiao Tung University, Hsinchu, Taiwan 30010, Republic of China. E-mail: htchiu@nctu.edu.tw; Fax: +886-3-5723764*

[b]*Department of Materials Science and Engineering, National Tsing Hua University, Hsinchu, Taiwan 30013, Republic of China*

Experimental

Syntheses

Porous TiO$_2$ (PT). In a typical experiment, to TiCl$_{4(l)}$ (3.3 mL, 30.03 mmol) in a N$_2$-filled three-necked flask at a 0 °C, absolute C$_2$H$_5$OH$_{(l)}$ (14 mL) in a pressure-equalizing dropping funnel was added drop-by-drop (**Caution:** a large amount of HCl$_{(g)}$ was generated simultaneously). Then, NH$_4$OH$_{(aq.)}$ (25%) was added so that the pH value of the reaction mixture was adjusted to around 2. To this mixture, instant yeast (10 g), purchased from a local bakery supplier and suspended in an aqueous glucose solution (0.4 M, 20 mL), was mixed. The slurry was stirred and allowed to react at room temperature for 20 h. After the light-yellow product was dried at 80 °C overnight, the as-obtained dark brown solid was annealed at 400 °C under vacuum for 4 h to remove volatile byproducts. A black powder was isolated and oxidized at 400 °C in O$_{2(g)}$ environment for 4 h to offer a white solid product (2.38 g, 99.2% yield based on TiCl$_4$). For comparison, a reference sample was also prepared *via* a similar route without the addition of yeast and glucose.

Carbonized PT (C-PT). The as-prepared PT was further infiltrated with a thin layer of carbon at 400 °C by chemical vapour deposition (CVD) using CH$_3$OH$_{(g)}$ as the precursor and Ar$_{(g)}$ (30 sccm) as the carrier gas for 10 h. C-PT was isolated as a black solid. For comparison, C-PT-2 was also prepared under the same reaction condition for 4 h. Results of the characterizations of PT, C-PT, C-PT-2, and the reference sample are summarized in Table 1.

Characterizations

Morphology and structure of the samples were investigated by a JEOL JSM-7401F field emission scanning electron microscope (SEM) at 10 kV and a JEOL JEM-2010 transmission electron microscope (TEM) at 200 kV. Crystallinity of the samples, taped on the notch of a square plastic holder, was examined by a Bruker AXS D8 Advance X-ray diffractometer (XRD, scan range 10°–80°) using Cu Kα radiation. Specific surface areas and pore size distributions of the samples were measured by N$_{2(g)}$ adsorption–desorption analyses using an ASAP2020 system. Raman spectra were measured by a portable Raman spectrometer MiniRam II at 785 nm. Elemental analyses (EA) were measured by an Elementar vario EL cube system. Thermogravimetric analyses (TGA, room temperature to 600 °C, heating rate 10 °C min^{-1}) were performed under O$_{2(g)}$ (40 mL min^{-1}) by using a TA Instruments TGA-Q50.

Electrochemical measurements

Typical working electrodes were fabricated by using the following steps. After the as-fabricated TiO$_2$ powders were ball-milled, a slurry was prepared by mixing the processed TiO$_2$ (80 wt%), the carbon black conducting agent (Super P®, 10 wt%), the polyvinylidene fluoride (PVDF) binder (10 wt%), and the *N*-methyl-2-pyrrolidone (NMP) electrolyte. The as-prepared slurry was coated on a piece of Cu foil (thickness: 50 μm). The loaded material was estimated by weighing after the electrode was dried at 110 °C for 24 h in a vacuum oven to remove the solvent. Then, it was roll-pressed. The electrode was assembled with a piece of Li metal foil as the counter and reference electrode, a slice of Celgard 2400 membrane (pore size: 20 μm) as the cell separator, and LiClO$_4$ (1 M) in a solution of ethylene carbonate and diethyl carbonate (1 : 1 mixture by volume) as the electrolyte into coin cells (CR2032) in a dry-room. Cyclic voltammetry (CV) experiments were measured with a CHI 6081C electrochemical workstation (1–3 V, 0.1 mV s^{-1}). The discharge/charge tests were measured using an AcuTech BAT-750 battery testing system at a constant current density with cutoff voltages 3 V to 1 V. Electrochemical impedance spectroscopic (EIS) studies were performed on a CHI 6081C (0.1 Hz–100 kHz at 5 mV).

Results and discussions

According to our previous work, TiO$_2$ with both macro- and mesoporous structures demonstrated improved capacity for Li-ion batteries.[39] Thus, in this study, TiO$_2$ with both macro- and mesopores was prepared *via* a simple sol–gel method by using TiCl$_{4(l)}$ as the precursor and yeast and glucose as the sacrificial templates. TiCl$_{4(l)}$ was reacted with absolute C$_2$H$_5$OH$_{(l)}$ under the nitrogen atmosphere first and gently mixed with NH$_4$OH$_{(aq.)}$ to avoid the violent reaction reported in literature.[40] Also, *via* our route, less HCl$_{(g)}$ was generated. Then, instant yeast suspended in an aqueous glucose solution was mixed with the as-prepared precursor to provide the source of the pores. After work up at 400 °C, the PT product was isolated. The SEM image in Fig. 1(a) shows the spongy-like morphology of PT. Sizes of the pores displayed in Fig. 1(b) are 2–3 μm. This agrees well with the sizes of the yeast cell templates. Interestingly, PT showed a spongy-like structure while the TiO$_2$ prepared in our previous work displayed a channel-like morphology.[39] Although the bio-

Table 1 TiO$_2$ samples investigated for the electrode in LIB

Sample	Templates	Carbon coating[a] (h)	Carbon content[b] (wt%)	BET surface area (m^2 g^{-1})	Pore size Macro (μm)	Meso (nm)	Grain size[c] (nm)	Phase
PT	Yeast, glucose	—	—	82.8	2.5–3	4–51	11.2	Anatase
C-PT	Yeast, glucose	10	7.42	52.7	2.5–3	6–70	11.2	Anatase
C-PT-2	Yeast, glucose	4	4.81	57.6	2.5–3	6–50	11.1	Anatase
Reference	—	—	—	78.1	—	6–12	15.9	Anatase

[a] PT reacted with CH$_3$OH$_{(g)}$ in Ar$_{(g)}$ (30 sccm) at 400 °C. [b] From EA data. [c] Calculated from XRD data by using Scherrer equation.
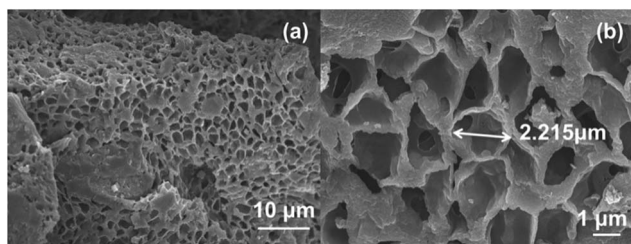
Fig. 1 (a) Low and (b) high magnification SEM images of PT.

ingredients, yeast and glucose, were the same in both studies, the TiO_2 precursors were different. In this study, $TiCl_{4(l)}$ was employed while in the previous case, $Ti(O^iPr)_{4(l)}$ (TTIP) was used. In the mild aqueous media containing TTIP, the yeast cells still maintained their vitality. Thus, CO_2 bubbles from the cell respiration and the physical cell structures acted cooperatively to assist the formation of the channel-like TiO_2. However, in this case, yeast cells were deceased due to the highly acidic environment, caused by the formation of $HCl_{(g)}$ from the reaction between $TiCl_{4(l)}$ and $C_2H_5OH_{(l)}$. Consequently, the yeast cell walls acted only as the templates to assist the formation of the spongy-like macroporous structure.

The TEM images of PT, shown in Fig. 2(a) and (b), display aggregates of nanoparticles. The small voids observed among the particles in Fig. 2(a) suggest the presence of mesopores within the material. In the high-resolution TEM (HRTEM) image, Fig. 2(b), fringes with a lattice spacing 0.35 nm are observed. This is in good agreement with the *d*-spacing associated with anatase TiO_2 (101) planes, 0.35 nm (JCPDS 89-4921). Fig. 2(c) reveals the selected area electron diffraction (SAED) pattern from the sample shown in Fig. 2(a). The diffraction rings indicate that the sample is polycrystalline. They are
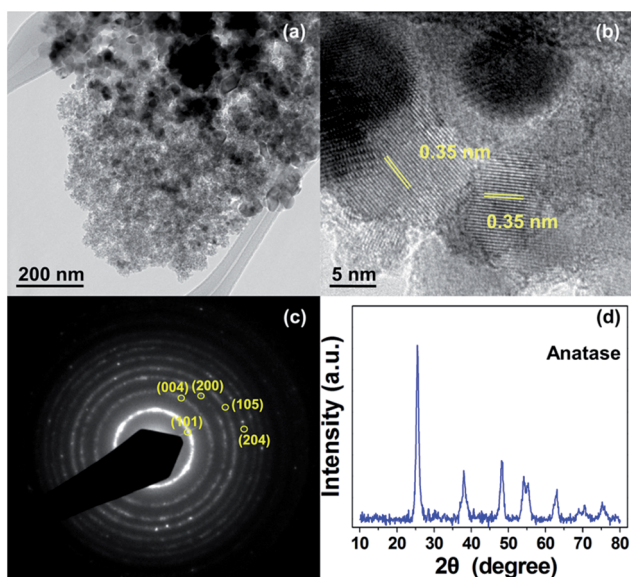
assigned to (101), (004) and (200) planes of anatase TiO_2. Moreover, the XRD pattern of PT displayed in Fig. 2(d) shows characteristic 2θ peaks at 25.3°, 37.8°, 48.1°, 53.9°, 55.1°, 62.8°, 68.8°, 70.4° and 75.2°. They are assigned to (101), (004), (200), (105), (211), (204), (116), (220) and (215) planes of anatase TiO_2 (JCPDS 89-4921).

Nitrogen adsorption–desorption analyses were carried out to offer the specific surface areas and pore size distributions of the samples *via* Brunauer–Emmett–Teller (BET) equation and Barrett–Joyner–Halenda (BJH) theory. Fig. 3 summarizes their isotherm and pore size distribution data. The isotherm displayed in Fig. 3(a) reveals type IV hysteresis loop suggesting capillary condensation behaviour at high pressures. From the data, the specific surface area of PT is estimated to be 82.8 m² g⁻¹. The result confirms that in addition to the macroporous structure, mesopores also exist within PT. Together, they provide a broad pore size distribution 4–51 nm with a maximum at 13 nm (the data were determined from the reasonable BJH scale 2–60 nm with the pore volume higher than 1 cm³ g⁻¹ nm⁻¹), as shown in the inset in Fig. 3(a). In Fig. 3(b), the reference sample (see Fig. S1 in the ESI†), prepared without the presence of yeast and glucose, reveals a similar specific surface area 78.1 m² g⁻¹ but a much narrow pore size distribution 6–12 nm and a maximum at 9 nm. The observed hysteresis loop indicates that capillary condensation occurred at high pressures. The data suggest that only mesopores existed in the reference sample. Because glucose and yeast were not added during the preparation, no macropores existed in this case. The related characterization data are summarized in Table 1.

A reaction pathway is presented in Scheme 1 to summarize the formation of PT. We suggest that various titanium hydrates would be formed through hydrolysis of $TiCl_4$. These hydrates could react with the hydroxyl groups of glucose *via* condensation reactions. Thus, the glucose molecules may be viewed as the centers for the formation of titanate precursors. Carboxyl and phosphate groups on the yeast cell surface provide negatively charged templates. Positively charged titanium hydrates combine with the yeast cells and hydrolyzed in the glucose solution to form titanates. On the other hand, the sample prepared without yeast did not show the presence of macropores. Also, the sample prepared without glucose showed much less mesopores because it displayed a distribution curve beyond
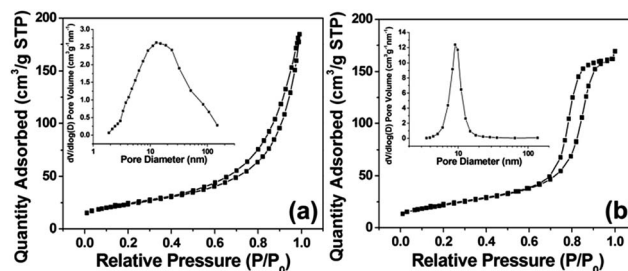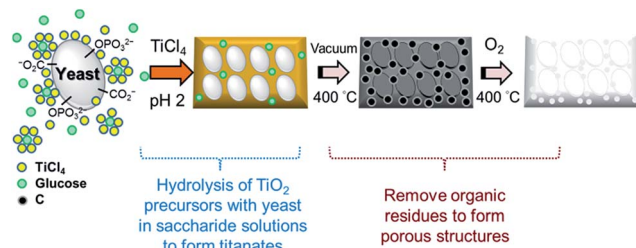

Fig. 2 (a) TEM and (b) HRTEM images of PT. (c) SAED of (a). (d) XRD pattern of PT.

Fig. 3 N₂ adsorption–desorption isotherms of (a) PT and (b) reference samples. The reference sample was prepared *via* the same route of PT but without the presence of yeast and glucose. Inset: pore size distributions of the materials.

Scheme 1 Proposed pathway of the formation of PT.

the reasonable scale predicted by BJH theory. Thus, we propose that the cells and the glucose molecules acted together as the pore generation templates. Similar pathways for pore generation through organism–inorganic matrix interactions were proposed.[33,35] After the hybrid mixture is processed at 400 °C under vacuum, the cells and the glucose molecules are either vapourized to leave empty spaces or decomposed into nanosized carbon particles. After further treatment at 400 °C in $O_{2(g)}$, all carbon residues are oxidized to offer mesopores while the titanate crystallizes into anatase TiO_2. On the other hand, we also tried direct O_2 treatment at 400 °C. The as-obtained TiO_2 product showed a smaller specific surface area, 42 m² g⁻¹. The value is about half of the reported one for sample PT, 82.8 m² g⁻¹. In summary, the porous structure is generated due to yeast cells, glucose molecules, and various decomposition byproducts. Together, they offer the broad mesoporous size distribution observed in Fig. 3(a).

According to previous studies, it is known that anatase TiO_2 is one of the promising anode materials for Li-ion battery. TiO_2 is a typical Li ion intercalation material with a small volume change (<4%) during the discharge–charge cycling. This differs from other anode materials such as graphite, Si, and Sn. They show obvious volume changes (10–400%) during the cycling.[9,41–43] The negligible lattice changes of TiO_2-based structures during Li ion intercalation and de-intercalation are responsible for enhanced structural stability and extended cycle life. However, one of the drawbacks of TiO_2 materials is their poor electron conductivity. Some literatures suggest that carbon coating on TiO_2 reduces the inner resistance of the anode. Consequently, the battery performance may be enhanced.[18,20] Therefore, the as-prepared PT was further coated with a layer of carbon by CVD to produce C-PT. As shown in the HRTEM image in Fig. 4(a), a thin layer (2 nm) of amorphous carbon,
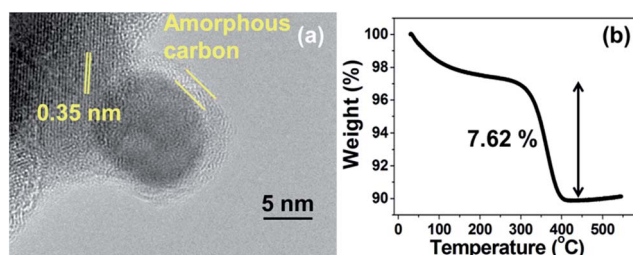
determined by energy dispersive X-ray spectroscopy (EDX, Fig. S2 in the ESI†), is observed for C-PT. The Raman spectrum displays characteristic peaks of amorphous carbon at 1350 and 1550 cm⁻¹ (Fig. S3 in the ESI†). The overall morphology and crystal structure of C-PT are the same as those of PT (Fig. S4 and S5†). Covering PT with the carbon layer reduces the specific surface area of C-PT to 52.7 m² g⁻¹, as measured by the nitrogen adsorption–desorption experiment (Fig. S6 in the ESI†). The EA result indicates that C-PT contained 7.42 wt% carbon. The TGA curve of C-PT in $O_{2(g)}$ shows an obvious weight loss from 200 °C to 500 °C in Fig. 4(b). The weight loss below 200 °C is attributed to the evaporation of adsorbed gases and moisture. As a result, he carbon content in C-PT is determined to be 7.62 wt%. This agrees well with the EA result. The electrochemical behaviours of anatase TiO_2 were reported in previous research articles.[44,45] In this study, TiO_2/Li half-cells were assembled from the samples listed in Table 1. As reported in literature, Li⁺ insertion and extraction in anatase TiO_2 occurs according to the following equation.[46,47]

$$TiO_2 + xLi^+ + xe^- \rightleftarrows Li_xTiO_2 \ (x \leq 1) \tag{1}$$

Commonly, within a potential window 3–1 V, TiO_2 is transformed into $Li_{0.5}TiO_2$ ($x = 0.5$) at 1.7 V. Below 1.7 V, the formation of Li_xTiO_2 ($x > 0.5$) becomes very slow. The process is efficient only for TiO_2 with small particle sizes and high surface areas.[48] Thus, the reversible capacity reported for bulk anatase TiO_2 is 167 mA h g⁻¹ at $x = 0.5$.[49] Fully lithiated Li_xTiO_2 ($x = 1$) could be obtained from nanosized anatase TiO_2 (7 nm).[50] Under this situation, the theoretical capacity of TiO_2, 334 mA h g⁻¹, is achieved. Since the particle sizes in our samples are in the nm scale range, we anticipate that they may achieve x values much above 0.5.

To confirm the behaviour of the electrode materials during the discharge–charge process, CV experiments were performed. Fig. 5 and S7 in the ESI† show representative CV curves (3 to 1 V) of the obtained C-PT, PT and the reference sample. Two current peaks at ca. 1.7 V (cathodic sweep) and 2.0 V (anodic sweep) are observed for all samples. They are the signature of Li ion
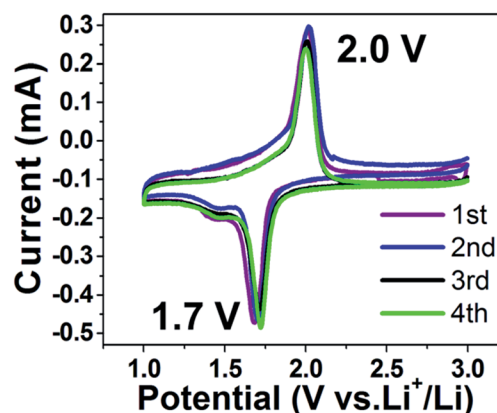

Fig. 4 (a) HRTEM image and (b) TGA of C-PT.

Fig. 5 Continuous CV scans of C-PT (scan rate 0.1 mV s⁻¹).

intercalation and de-intercalation processes in the anatase framework.[44] Fig. 6 presents the rate capabilities of the TiO$_2$ samples listed in Table 1. The corresponding data from the first, second, 6th, 7th, 79th, and 80th cycles are shown in Fig. S8.† Due to the presence of mesopores and trace amounts of surface OH and H$_2$O groups on the TiO$_2$ nanoparticles, the initial reaction processes were irreversible.[51,52] Thus, the apparent high capacities, faded further in the subsequent cyclings, exceed the theoretical value and should be ignored.[53,54] After the performance stabilized at the 7th cycle, the discharge capacity of PT is found to be 138 mA h g^{-1} at 0.5 C (1 C = 334 mA g^{-1}). After continuous cyclings at varied rates (from 0.5 C to 20 C, then back to 0.1 C), it retains 160 mA h g^{-1} at the 80th cycle. C-PT shows great improvements. For example, its rate capacities are 321 mA h g^{-1}, 265 mA h g^{-1}, 180 mA h g^{-1}, and 142 mA h g^{-1} at 0.5 C, 1 C, 5 C, and 10 C, respectively. Moreover, it maintains good cycling stability. After discharged and charged at various rates for 80 cycles, a respectable value 318 mA h g^{-1} is still observed at 0.1 C. The result is 95% of the theoretical capacity of TiO$_2$. The origin of the superior performance of C-PT is attributed to the assistance from the layered carbon network on the TiO$_2$. Another sample, C-PT-2, prepared with a less carbon layer coating time than C-PT had, demonstrates inferior performance, as displayed in Fig. 6. Other literature reports employing nanosized TiO$_2$ showed observations similar to our findings.[55–57]

Fig. S9† presents the rate capacities of another device composed of C-PT. Because all devices were hand-assembled, performance variations existed among devices. Although its capacities fade rapidly in the initial cycles, they stabilize after more cycles. After 100 cycles, the device maintains 111 mA h g^{-1}, which is 83% of the capacity at the sixth cycle. Compared to other reports involving various TiO$_2$ morphologies listed in Table S1,† C-PT is among the best ones demonstrating excellent capability at high discharge–charge rates.[18,19,45–47,58–62] The reference sample, prepared without the presence of glucose and

yeast, shows the same surface area as that of PT. However, its capacity fades rapidly at high discharge rates. This is attributed to the absence of macroporous structure in this sample. The presence of 3D spongy-like structure probably provides more open spaces for the intercalation/deintercalation of Li ions. As a result, the intercalation/deintercalation of Li ions becomes less accessible even though the surface area of the reference sample is still high.[39,63] In C-PT, in addition to the macro/mesoporous structure, a C layer also exists. This network may enhance the battery performance also. Our results are comparable to several recent observations employing electrodes composed of other TiO$_2$ with both meso- and macropores fabricated using different strategies.[63,64]

To realize why the performance of C-PT was enhanced in this work, electron transport properties of the samples PT, C-PT, and the reference one are compared using the information derived from the EIS data.[65,66] Fig. S10(a) in the ESI† reveals the impedance plots of PT, C-PT and the reference sample before the cyclings. The impedance spectra at high frequencies correspond to the charge transfer resistance at the interface between the electrode and the electrolyte. The reference sample shows the largest semicircle, which means that it has the largest charge transfer resistance. From Fig. S10(b),† the Warburg factor (σ) could be calculated from the slope by using eqn S1.† The impedance spectra at the low frequencies correspond to Warburg diffusion. They provide the diffusion abilities of Li ions in the electrode. The diffusion coefficient D of Li ion could be calculated from the plot in the low frequency region in Fig. S10(a)† using the Warburg diffusion equation (eqn S2 in the ESI†). The results are summarized in Table S2.† Clearly, C-PT shows the highest D value 6.36×10^{-13} cm^2 s^{-1} among the samples. It is higher than the D value of anatase reported in literature, approximately 2×10^{-13} cm^2 s^{-1}.[67] Fig. S11† shows the impedance plots of C-PT before and after 10 discharge–charge cycles. The diameter of the semicircle after the cycling decreases, as presented in Fig. S11(a).† This suggests that the charge transfer resistance R_{ct} decreases after the cycling. This might be caused by the infiltration of the electrolyte solution into the nanostructured electrode to decrease the polarization. After the cycling, the D value for C-PT is increased to 1.42×10^{-11} cm^2 s^{-1}. This suggests that Li ions diffuse much easier in the C-PT based battery after the cycling. As reported in literature, rapid Li ion diffusion properties are responsible for high rate capability Li-ion batteries.[1] In our case, the combination of low R_{ct} and high D values of the C-PT electrode provides the excellent battery performance.

Conclusions

In summary, unique macroporous anatase TiO$_2$ (pore size: 2.5–3 μm) with mesopores (4–51 nm), sample PT, was successfully synthesized *via* a sol–gel route by combining yeast and glucose as the biotemplates. They worked cooperatively to offer the final porous structure. The porous morphology provided high specific surface areas and open spaces. The material functioned as an electrode material for Li-ion battery with good capacity retention due to the effortless intercalation/deintercalation of Li
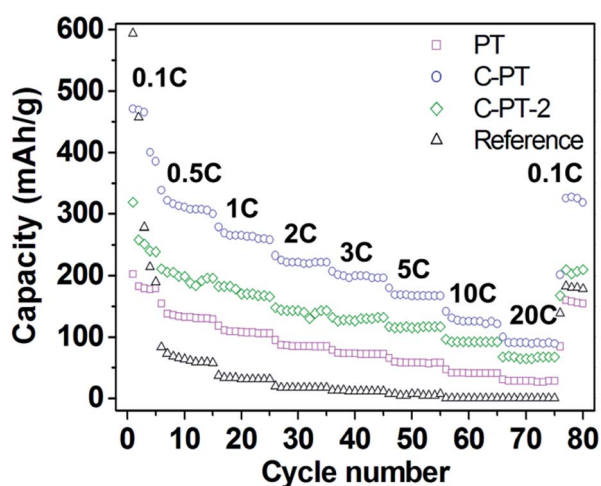

Fig. 6 Rate performance of samples at different current rates for 80 cycles. All measurements were conducted with a voltage window 1–3 V (1 C = 334 mA g^{-1}).

ions. In order to enhance the electrode performance, carbon-coated PT, sample C-PT, was prepared by CVD. The electrode demonstrated excellent cycling stability and high rate performance. The cycling capacities of C-PT were enhanced significantly. They increased to 180 mA h g^{-1} and 142 mA h g^{-1} at 5 C and 10 C, respectively, and 318 mA h g^{-1} at 0.1 C after 80 discharge–charge cycles at various rates. The performance of the battery constructed from C-PT is one of the best among the porous anatase TiO$_2$ electrode materials listed in Table S1 in the ESI.† The coated-carbon network improved the electrochemical property of the porous TiO$_2$ greatly. The hierarchical porous structure demonstrated high diffusion coefficient, an essential character for high rate capability in rechargeable batteries. Our unique material showed excellent cycle stability and rate efficiency. These qualities are important for the advancement of the application of anatase TiO$_2$ in the Li-ion battery technology. The concepts developed in this study might be extended to other electrode materials for energy storage devices.

Acknowledgements

Notes and references

1 B. Kang and G. Ceder, *Nature*, 2009, **458**, 190–193.
2 J. M. Tarascon and M. Armand, *Nature*, 2001, **414**, 359–367.
3 Z. G. Yang, D. Choi, S. Kerisit, K. M. Rosso, D. H. Wang, J. Zhang, G. Graff and J. Liu, *J. Power Sources*, 2009, **192**, 588–598.
4 R. Marchand, L. Brohan and M. Tournoux, *Mater. Res. Bull.*, 1980, **15**, 1129–1133.
5 K. Saravanan, K. Ananthanarayanan and P. Balaya, *Energy Environ. Sci.*, 2010, **3**, 939–948.
6 W. J. H. Borghols, D. Lutzenkirchen-Hecht, U. Haake, W. Chan, U. Lafont, E. M. Kelder, E. R. H. van Eck, A. P. M. Kentgens, F. M. Mulder and M. Wagemaker, *J. Electrochem. Soc.*, 2010, **157**, A582–A588.
7 J. Yan, B. J. Xia, Y. C. Su, X. Z. Zhou, J. Zhang and X. G. Zhang, *Electrochim. Acta*, 2008, **53**, 7069–7078.
8 D. Deng, M. G. Kim, J. Y. Lee and J. Cho, *Energy Environ. Sci.*, 2009, **2**, 818–837.
9 K. C. Hsu, C. E. Liu, P. C. Chen, C. Y. Lee and H. T. Chiu, *J. Mater. Chem.*, 2012, **22**, 21533–21539.
10 E. Baudrin, S. Cassaignon, M. Koesch, J. P. Jolivet, L. Dupont and J. M. Tarascon, *Electrochem. Commun.*, 2007, **9**, 337–342.
11 Y. S. Hu, L. Kienle, Y. G. Guo and J. Maier, *Adv. Mater.*, 2006, **18**, 1421–1426.
12 D. H. Wang, D. W. Choi, J. Li, Z. G. Yang, Z. M. Nie, R. Kou, D. H. Hu, C. M. Wang, L. V. Saraf, J. G. Zhang, I. A. Aksay and J. Liu, *ACS Nano*, 2009, **3**, 907–914.
13 Y. G. Guo, J. S. Hu and L. J. Wan, *Adv. Mater.*, 2008, **20**, 4384.

14 M. Okubo, E. Hosono, J. Kim, M. Enomoto, N. Kojima, T. Kudo, H. S. Zhou and I. Honma, *J. Am. Chem. Soc.*, 2007, **129**, 7444–7452.
15 A. D. Robertson, A. R. Armstrong and P. G. Bruce, *Chem. Mater.*, 2001, **13**, 2380–2386.
16 A. S. Arico, P. Bruce, B. Scrosati, J. M. Tarascon and W. Van Schalkwijk, *Nat. Mater.*, 2005, **4**, 366–377.
17 L. J. Fu, H. Liu, C. Li, Y. P. Wu, E. Rahm, R. Holze and H. Q. Wu, *Solid State Sci.*, 2006, **8**, 113–128.
18 L. X. Zeng, C. Zheng, L. C. Xia, Y. X. Wang and M. D. Wei, *J. Mater. Chem. A*, 2013, **1**, 4293–4299.
19 M. H. Ryu, K. N. Jung, K. H. Shin, K. S. Han and S. K. Yoon, *J. Phys. Chem. C*, 2013, **117**, 8092–8098.
20 P. C. Chen, M. C. Tsai, H. C. Chen, I. N. Lin, H. S. Sheu, Y. S. Lin, J. G. Duh, H. T. Chiu and C. Y. Lee, *J. Mater. Chem.*, 2012, **22**, 5349–5355.
21 A. R. Studart, U. T. Gonzenbach, E. Tervoort and L. J. Gauckler, *J. Am. Ceram. Soc.*, 2006, **89**, 1771–1789.
22 J. Y. Huang, X. D. Wang and Z. L. Wang, *Nano Lett.*, 2006, **6**, 2325–2331.
23 S. Sotiropoulou, Y. Sierra-Sastre, S. S. Mark and C. A. Batt, *Chem. Mater.*, 2008, **20**, 821–834.
24 K. J. C. van Bommel, A. Friggeri and S. Shinkai, *Angew. Chem., Int. Ed.*, 2003, **42**, 980–999.
25 T. Nomura, Y. Morimoto, H. Tokumoto and Y. Konishi, *Mater. Lett.*, 2008, **62**, 3727–3729.
26 B. Bai, P. P. Wang, L. Wu, L. Yang and Z. H. Chen, *Mater. Chem. Phys.*, 2009, **114**, 26–29.
27 Z. Schnepp, W. Yang, M. Antonietti and C. Giordano, *Angew. Chem., Int. Ed.*, 2010, **49**, 6564–6566.
28 D. L. Yang, T. X. Fan, D. Zhang, J. Zhu, Y. Wang, B. Du and Y. X. Yan, *Chem.–Eur. J.*, 2013, **19**, 4742–4747.
29 N. Shi, X. H. Li, T. X. Fan, H. Zhou, J. A. Ding, D. Zhang and H. X. Zhu, *Energy Environ. Sci.*, 2011, **4**, 172–180.
30 J. J. Yan, G. J. Wu, L. D. Li, A. M. Yu, X. H. Sun and N. J. Guan, *J. Nanosci. Nanotechnol.*, 2010, **10**, 5767–5775.
31 M. Numata, K. Sugiyasu, T. Hasegawa and S. Shinkai, *Angew. Chem., Int. Ed.*, 2004, **43**, 3279–3283.
32 S. Y. Chia, J. Urano, F. Tamanoi, B. Dunn and J. I. Zink, *J. Am. Chem. Soc.*, 2000, **122**, 6488–6489.
33 W. He, S. P. Yan, Y. J. Wang, X. D. Zhang, W. J. Zhub, X. Y. Tian, X. A. Sun and X. X. Han, *J. Alloys Compd.*, 2009, **477**, 657–660.
34 W. He, W. J. Zhou, Y. J. Wang, X. D. Zhang, H. S. Zhao, Z. M. Li and S. P. Yan, *Mater. Sci. Eng., C*, 2009, **29**, 1348–1350.
35 J. J. Cui, W. He, H. T. Liu, S. J. Liao and Y. Z. Yue, *Colloids Surf., B*, 2009, **74**, 274–278.
36 W. He, J. J. Cui, Y. Z. Yue, X. D. Zhang, X. Xia, H. Liu and S. W. Lui, *J. Colloid Interface Sci.*, 2011, **354**, 109–115.
37 H. Adwan, B. Fuller, C. Seldon, B. Davidson and A. Seifalian, *J. Biomater. Appl.*, 2013, **28**, 250–261.
38 M. Lin, X. Li, W. Zhang and X. Ying, *J. Appl. Polym. Sci.*, 2013, **127**, 2067–2073.
39 Y. C. Chang, C. Y. Lee and H. T. Chiu, *ACS Appl. Mater. Interfaces*, 2014, **6**, 31–35.

40 H. I. Hsiang and S. C. Lin, *Mater. Sci. Eng., A*, 2004, **380**, 67–72.

41 N. A. Kaskhedikar and J. Maier, *Adv. Mater.*, 2009, **21**, 2664–2680.

42 D. Shao, D. P. Tang, Y. J. Mai and L. Z. Zhang, *J. Mater. Chem. A*, 2013, **1**, 15068–15075.

43 Y. Yu, L. Gu, C. B. Zhu, S. Tsukimoto, P. A. van Aken and J. Maier, *Adv. Mater.*, 2010, **22**, 2247–2250.

44 P. Kubiak, T. Fröschl, N. Hüsing, U. Hörmann, U. Kaiser, R. Schiller, C. K. Weiss, K. Landfester and M. Wohlfahrt-Mehrens, *Small*, 2011, **7**, 1690–1696.

45 D. Zhang, M. Wen, P. Zhang, J. Zhu, G. Li and H. Li, *Langmuir*, 2012, **28**, 4543–4547.

46 J. S. Chen, Y. L. Tan, C. M. Li, Y. L. Cheah, D. Luan, S. Madhavi, F. Y. C. Boey, L. A. Archer and X. W. Lou, *J. Am. Chem. Soc.*, 2010, **132**, 6124–6130.

47 Z. Wang and X. W. Lou, *Adv. Mater.*, 2012, **24**, 4124–4129.

48 J. Wang, J. Polleux, J. Lim and B. Dunn, *J. Phys. Chem. C*, 2007, **111**, 14925–14931.

49 D. W. Murphy, R. J. Cava, S. M. Zahurak and A. Santoro, *Solid State Ionics*, 1983, **9–10**, 413–417.

50 M. Wagemaker, W. J. H. Borghols and F. M. Mulder, *J. Am. Chem. Soc.*, 2007, **129**, 4323–4327.

51 M.-C. Tsai, J.-C. Chang, H.-S. Sheu, H.-T. Chiu and C.-Y. Lee, *Chem. Mater.*, 2009, **21**, 499–505.

52 Y. S. Hu, P. Adelhelm, B. M. Smarsly, S. Hore, M. Antonietti and J. Maier, *Adv. Funct. Mater.*, 2007, **17**, 1873–1878.

53 H. Xiong, H. Yildirim, E. V. Shevchenko, V. B. Prakapenka, B. Koo, M. D. Slater, M. Balasubramanian, S. K. R. S. Sankaranarayanan, J. P. Greeley, S. Tepavcevic, N. M. Dimitrijevic, P. Podsiadlo, C. S. Johnson and T. Rajh, *J. Phys. Chem. C*, 2012, **116**, 3181–3187.

54 W. J. H. Borghols, D. Lützenkirchen-Hecht, U. Haake, W. Chan, U. Lafont, E. M. Kelder, E. R. H. van Eck, A. P. M. Kentgens, F. M. Mulder and M. Wagemaker, *J. Electrochem. Soc.*, 2010, **157**, A582–A588.

55 G. Li, Z. Zhang, H. Peng and K. Chen, *RSC Adv.*, 2013, **3**, 11507–11510.

56 B. Wang, H. Xin, X. Li, J. Cheng, G. Yang and F. Nie, *Sci. Rep.*, 2014, **4**, 3729.

57 H. Ming, X. Li, L. Su, M. Liu, L. Jin, L. Bu, Z. Kang and J. Zheng, *RSC Adv.*, 2013, **3**, 3836–3839.

58 K. Wang, M. Wei, M. A. Morris, H. Zhou and J. D. Holmes, *Adv. Mater.*, 2007, **19**, 3016–3020.

59 S. Ding, J. S. Chen, Z. Wang, Y. L. Cheah, S. Madhavi, X. Hu and X. W. Lou, *J. Mater. Chem.*, 2011, **21**, 1677–1680.

60 J. Ye, W. Liu, J. Cai, S. Chen, X. Zhao, H. Zhou and L. Qi, *J. Am. Chem. Soc.*, 2010, **133**, 933–940.

61 Y. Ma, G. Ji, B. Ding and J. Y. Lee, *J. Mater. Chem.*, 2012, **22**, 24380–24385.

62 J. Shen, H. Wang, Y. Zhou, N. Ye, G. Li and L. Wang, *RSC Adv*, 2012, **2**, 9173–9178.

63 H. Wang, H. Yang, L. Lu, Y. Zhou and Y. Wang, *Dalton Trans.*, 2013, **42**, 8781–8787.

64 H. Liu, Z. Bi, X.-G. Sun, R. R. Unocic, M. P. Paranthaman, S. Dai and G. M. Brown, *Adv. Mater.*, 2011, **23**, 3450–3454.

65 Y. Cui, X. L. Zhao and R. S. Guo, *Electrochim. Acta*, 2010, **55**, 922–926.

66 X. Du, W. He, X. Zhang, Y. Yue, H. Liu, X. Zhang, D. Min, X. Ge and Y. Du, *J. Mater. Chem.*, 2012, **22**, 5960–5969.

67 L. Kavan, M. Grätzel, S. E. Gilbert, C. Klemenz and H. J. Scheel, *J. Am. Chem. Soc.*, 1996, **118**, 6716–6723.